J. Fluid Mech. (1999), *vol.* 380, *pp.* 59–80. Printed in the United Kingdom

Eddy fluxes and topography in stratified quasi-geostrophic models

By WILLIAM J. MERRYFIELD AND GREG HOLLOWAY

Institute of Ocean Sciences, Sidney, B.C., V8L 4B2, Canada

(Received 5 May 1997 and in revised form 16 August 1998)

Turbulent stratified flow over topography is studied using layered quasi-geostrophic models. Mean flows develop under random forcing, with lower-layer mean streamfunction positively correlated with topography. When friction is sufficiently small, upper-layer mean flow is weaker than, but otherwise resembles, lower-layer mean flow. When lower-layer friction is larger, upper-layer mean flow reverses and can exceed lower-layer mean flow in strength. The mean interface between layers is domed over topographic elevations. Eddy fluxes of potential vorticity and layer thickness act in the sense of driving the flow toward higher entropy. Such behaviour contradicts usual eddy parameterizations, to which modifications are suggested.

1. Introduction

Ocean models, particularly the coarse-resolution models used in climate studies, often do not explicitly resolve eddies. The performance of such models rests largely upon how well eddy transports are parameterized. The simplest approach of representing eddy fluxes by downgradient Fickian diffusion of temperature, salinity and momentum is demonstrably inadequate, and more realistic parameterizations are needed. Various alternatives have been proposed, sometimes premised upon Fickian or nearly-Fickian diffusion of potential vorticity or layer thickness.

The present paper seeks to examine effects of eddies, including flux–gradient relationships and mean-flow generation, in relatively simple stratified quasi-geostrophic models, with particular attention to the influence of topography. We consider two topographies, a ridge and a seamount, as well as different stratifications, locales of forcing, and dissipation formulae.

The quasi-geostrophic model is defined in § 2. Results, including mean flows, interface deformations and eddy fluxes, are described in § 3 and § 4. In § 5, we show the results to be qualitatively in accord with the notion that eddies drive the flow toward higher entropy. We discuss in § 6 how eddy parameterizations might be modified to better account for the joint influence of eddies, topography and stratification. Results are discussed in § 7 and summarized in § 8.

2. Model formulation

The equations describing two-layer quasi-geostrophic flow on an f-plane, with surface forcing $\mathscr{F}$ and dissipation D, are

$$\frac{\partial q_i}{\partial t} + J(\psi_i, q_i) = \mathscr{F}\delta_{i1} - D_i, \quad i = 1, 2, \tag{2.1}$$

where potential vorticity q_i and streamfunction ψ_i are related by

$$q_1 = \nabla^2\psi_1 + F_1(\psi_2 - \psi_1), \tag{2.2}$$

$$q_2 = \nabla^2\psi_2 + F_2(\psi_1 - \psi_2) + h, \tag{2.3}$$

with $F_i = f_0^2/g'H_i$. Here, f_0 is Coriolis parameter, H_i is mean thickness of layer i, g' is reduced gravity of the layer interface, $h = f_0(H_0 - H)/H_2$ where H is total depth and H_0 mean total depth, δ_{ij} is the Kroneker delta, ∇^2 is the horizontal Laplacian, and $J(A, B) = |\partial(A, B)/\partial(x, y)|$ is the Jacobian determinant with respect to horizontal coordinates (x, y).

Horizontal boundary conditions are periodic, and numerical solutions are obtained by Fourier spectral collocation, with dealiasing by the 2/3 rule (e.g. Canuto *et al.* 1988). Temporal integration is via a leapfrog scheme, with a trapezoidal step occasionally inserted to maintain numerical stability. The dissipation terms are represented by exponential integration factors.

The computational domain is 1024 km on a side, with grid spacing 8 km, corresponding to truncation wavenumber (after dealiasing) of 42 times the fundamental wavenumber k_0. Mean total depth H_0 is 4500 m, and the interface between layers has mean depth 900 m.

Forcing, random in time and space, is governed by a Markov process

$$\frac{\partial \mathscr{F}_{\boldsymbol{k}}}{\partial t} = -\frac{1}{\tau}\mathscr{F}_{\boldsymbol{k}} + G_{\boldsymbol{k}}(t), \tag{2.4}$$

where $\boldsymbol{k}$ is wavenumber, $G_{\boldsymbol{k}}(t)$ is a white noise process, and τ is a forcing timescale. The $G_{\boldsymbol{k}}(t)$ are selected from bi-Gaussian distributions having variances scaled by a one-dimensional power spectrum $\propto \exp[-(k - 3k_0)^2/k_0^2]$ over $k < 5k_0$, where $k = |\boldsymbol{k}|$.

Recognizing that dissipation in the oceans is poorly understood, we consider various dissipation laws D_i. In all cases, $D_2 = \nu_0\nabla^2\psi_2 + \nu_4\nabla^6\psi_2$, where ν_0 and ν_4 are coefficients of Rayleigh and biharmonic friction (e.g. Holland 1978). In the upper layer, we choose from

$$D_1 = \nu_4\nabla^6\psi_1 \qquad \text{(dissipation law I)}, \tag{2.5a}$$

$$D_1 = \nu_0\nabla^2\psi_1 + \nu_4\nabla^6\psi_1 \qquad \text{(dissipation law II)}, \tag{2.5b}$$

$$D_1 = \nu_0 q_1 + \nu_4\nabla^4 q_1 \qquad \text{(dissipation law III)}. \tag{2.5c}$$

We consider a sequence of model runs whose properties are summarized in tables 1–4. Runs R1–R4 and related ancillary runs have bumpy ridge topography and runs S1–S4 bumpy seamount topography, as described below. Deformation radius L_D is 20 km, a value representative of mid-latitude oceans (Emery, Lee & Magaard 1984), except in R1 and S1, for which $L_D = 5$ km. Runs R2–R4 and S2–S4 comprise sequences having increasing Rayleigh friction. All runs adopt upper-layer dissipation law I, except R2II (law II), and R2III (law III). In § 3.4 we consider additional runs in which forcing is barotropic, and in § 3.5 a run in which the ridge is smooth rather than bumpy.

Each run is integrated for approximately 80 years, as compared to a circulation timescale (domain width divided by typical velocity 10 cm s^{-1}) of order 100 days. Temporal means, determined by averaging over the final 50 years, will be indicated by overbars.

Parameter		Value
Domain size	L	1024 km
Grid	L/N	8 km
Cutoff wavenumber	k_1/k_0	42
Biharmonic friction	ν_4	3.5×10^{16} cm^4 s^{-1}
Mean ocean depth	H_0	4500 m
Mean interface depth	H_1	900 m
Coriolis parameter	f	10^{-4} s^{-1}
Forcing amplitude (r.m.s.)	$\mathscr{F}$	0.7×10^{-12} s^{-2}
Forcing timescale	τ	22 days

TABLE 1. Parameters common to all model runs

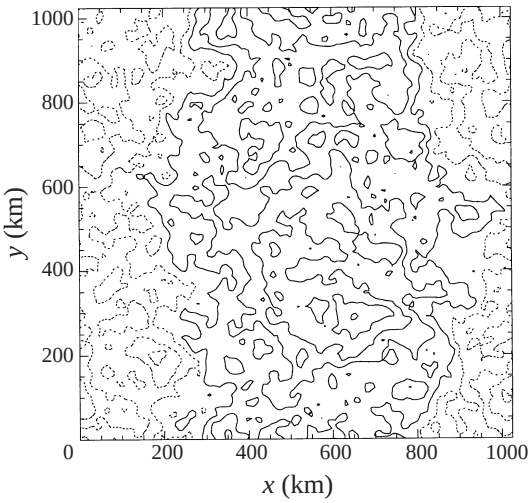

FIGURE 1. Ridge topography used in § 3. Solid contours denote regions above mean depth, and dashed contours regions below mean depth. Contour interval is 60 m.

3. Ridge results

We consider first a sinusoidal ridge with random topographic irregularities described by a power spectrum $\propto (k+4k_0)^{-2.5}$. Depths range from 4186 m to 4818 m, and the root-mean-square amplitude of roughness is 64 m (figure 1). Here the y-averaged component of forcing was set to zero to ensure mean flows paralleling the ridge are forced only by eddies, rather than by $\mathscr{F}$. Properties of these solutions are described in tables 2 and 3.

3.1. *Mean flows and interface deformations*

Runs R1–R4, R2II and R2III all exhibit strong bottom-layer mean flows, correlated with topography in the sense of anticyclonic circulation over bumps. In runs R1, R2, R2II and R2III, having smallest Rayleigh friction coefficient $\nu_0 = 0.5 \times 10^{-7}$ s^{-1}, upper-layer mean flow is similar to, though weaker than, lower-layer mean flow (figure 2). Upper-layer mean flow among these four runs is least attenuated in run R1 having $L_D = 5$ km, as is evident from the mean steady flow speeds $\langle \overline{u}_1 \rangle$ and $\langle \overline{u}_2 \rangle$ listed in table 2. These tendencies for topographically-correlated mean flow, increasingly attenuated upward for larger L_D, are much like those exhibited by models in which

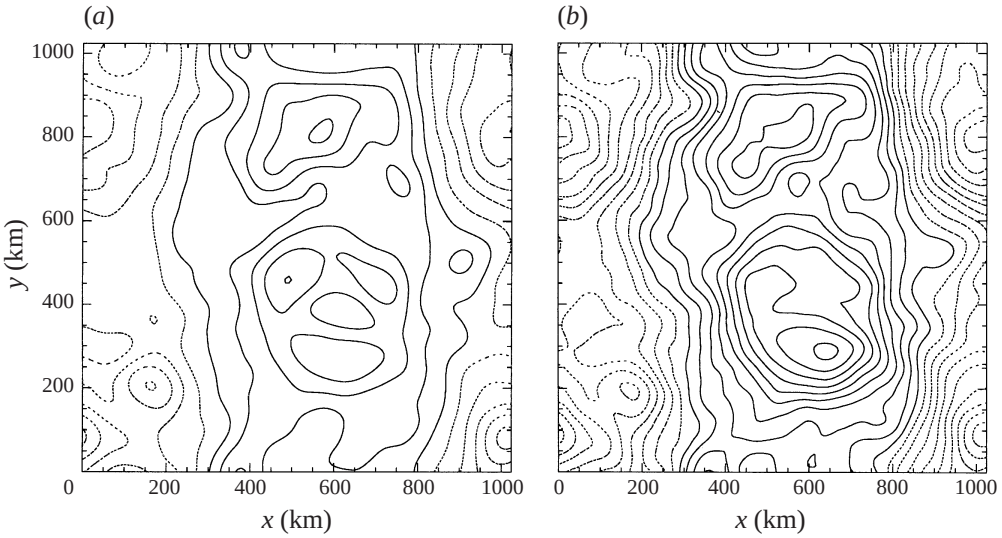

FIGURE 2. (*a*) Upper- and (*b*) lower-layer mean streamfunctions $\overline{\psi}_i$ for ridge run R2 having $\nu_0 = 0.5 \times 10^{-7}$ s^{-1}. Contour interval is 10^7 cm^2 s^{-1}. Solid contours are positive, and dashed contours negative.

Quantity	R1	R2	R3	R4	R2II	R2III
L_D (km)	5	20	20	20	20	20
ν_0 (s^{-1})	0.5×10^{-7}	0.5×10^{-7}	1.6×10^{-7}	5×10^{-7}	0.5×10^{-7}	0.5×10^{-7}
Dissipation law	I	I	I	I	II	III
$\langle u_1 \rangle$ (cm s^{-1}) [a]	3.7	6.6	8.1	8.4	5.4	4.4
$\langle u_2 \rangle$ (cm s^{-1}) [a]	3.6	4.4	2.7	1.5	3.8	3.4
$\langle \overline{u}_1 \rangle$ (cm s^{-1}) [b]	2.5	2.1	1.9	1.5	1.8	2.5
$\langle \overline{u}_2 \rangle$ (cm s^{-1}) [b]	2.7	3.6	1.5	0.44	3.1	2.9
$(\overline{C}_{\psi h})_1$	0.819	0.522	−0.330	−0.422	0.461	0.078
$(\overline{C}_{\psi h})_2$	0.844	0.885	0.638	0.208	0.882	0.889
$\overline{\Delta}_{\max} - \overline{\Delta}_{\min}$ (m)	281	183	242	157	162	150
ν_0/A	0.6	0.5	3.8	8.0	0.5	1.1
μ_1 [c]	52	22	16	17	25	9.7
μ_2 [c]	6.2	4.9	3.2	4.8	6.6	14

[a] $\langle u \rangle_i = \left\{ \dfrac{1}{L^2} \displaystyle\int_0^L \mathrm{d}x \int_0^L \mathrm{d}y \, \overline{\boldsymbol{u}_i \cdot \boldsymbol{u}_i} \right\}^{1/2}, \quad \boldsymbol{u}_i = (\partial_y \psi_i, -\partial_x \psi_i).$

[b] $\langle \overline{u} \rangle_i = \left\{ \dfrac{1}{L^2} \displaystyle\int_0^L \mathrm{d}x \int_0^L \mathrm{d}y \, \overline{\boldsymbol{u}}_i \cdot \overline{\boldsymbol{u}}_i \right\}^{1/2}, \quad \overline{\boldsymbol{u}}_i = (\partial_y \overline{\psi}_i, -\partial_x \overline{\psi}_i).$

[c] For corresponding inviscid runs, units of k_0^2.

TABLE 2. Properties of ridge runs R1–R4, R2II and R2III with upper-layer forcing

forcing and dissipation are absent (Salmon, Holloway & Hendershott 1976; Merryfield 1998).

This picture changes radically when Rayleigh friction ν_0 becomes larger: runs R3 and R4, for which $\nu_0 = 1.6 \times 10^{-7}$ s^{-1} and $\nu_0 = 5 \times 10^{-7}$ s^{-1}, exhibit reversed upper-layer mean flows, as is evident from the negative streamfunction-topography correlation coefficients $\overline{C}_{\psi h,1}$ in table 2. These mean flows are stronger than in the lower layer, as is seen by comparing the spatially-averaged mean-flow speeds $\langle \overline{u}_i \rangle$ in

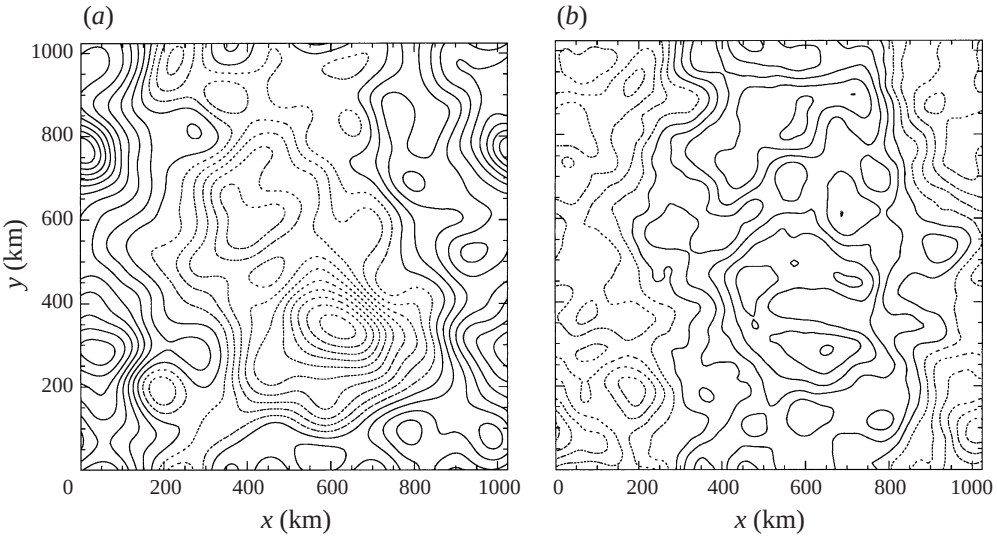

FIGURE 3. (*a*) Upper- and (*b*) lower-layer mean streamfunctions $\overline{\psi}_i$ for ridge run R3 having $\nu_0 = 1.6 \times 10^{-7}$ s^{-1}. Contour interval is 5×10^6 cm^2 s^{-1}. Solid contours are positive, and dashed contours negative.

the two layers (table 2). In the lower layer, increasing ν_0 damps the mean flow but does not alter its sense. Figure 3 shows the mean streamfunctions $\overline{\psi}_i$ for run R3.

The mean interface between layers is deformed by an amount

$$\overline{\Delta} = \frac{F}{f_0}(\overline{\psi}_2 - \overline{\psi}_1)H_0, \tag{3.1}$$

where $F \equiv f_0^2/g'H_0$. The interface is domed over the ridge in all cases. Total deformation $\overline{\Delta}_{\max} - \overline{\Delta}_{\min}$ is greatest (281 m) in run R1 having $L_D = 5$ km. Mean interface deformations for runs R1 and R2 are shown in figure 4.

3.2. *Eddy fluxes of potential vorticity*

Temporal-mean eddy fluxes of q_i perpendicular to the ridge axis and directed away from the crest are computed from $\langle \overline{\boldsymbol{u}_i q_i} \cdot \hat{\boldsymbol{x}} \rangle$, where the angle brackets denote averages over y, and $\hat{\boldsymbol{x}}$ is a unit vector pointing away from the crest. Figure 5 shows $\langle \overline{q} \rangle_1$ and $\langle \overline{q} \rangle_2$, together with the corresponding eddy fluxes, for runs R2, R2II, and R2III. In the model runs having dissipation law I, eddy fluxes are downgradient in the lower layer, and nearly vanishing in the upper layer. In run R2II having dissipation law II, eddy fluxes are downgradient in both layers. In run R2III having dissipation law III, eddy fluxes are downgradient in the lower layer, but countergradient in the upper layer.

3.3. *Eddy fluxes of layer thickness*

We have also computed fluxes of layer thickness anomaly Θ_i, where Θ_i is referenced to thickness in the absence of motion. From (2.2)–(2.3),

$$\Theta_i = -\frac{H_i}{f_0}(q_i - \nabla^2\psi_i - h\delta_{i2}), \tag{3.2}$$

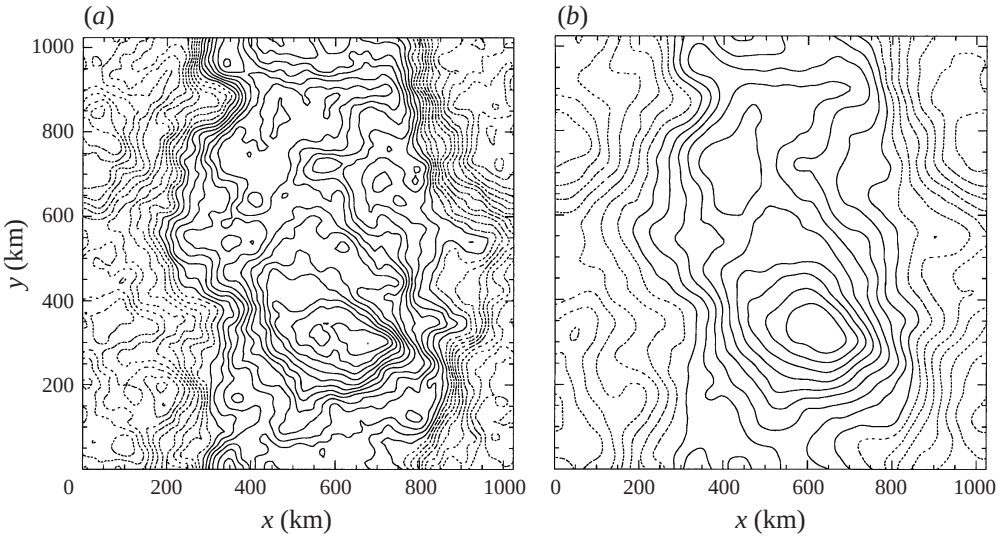

FIGURE 4. Mean interface deformations $\overline{\Delta}$ for ridge runs (*a*) R1 and (*b*) R2. Contour interval is 11 m. Solid contours denote upward displacement, and dashed contours downward displacement.

or $\Theta_1 = (f_0/g')(\psi_1 - \psi_2) = -\Theta_2$. By removing the topographic component, we ensure that column-integrated thickness anomaly vanishes (by virtue of the rigid top and bottom), and enable layer thickness to be identified with inverse density gradient.

In contrast to q_i, eddy fluxes of Θ_i cannot be computed from averages of $\boldsymbol{u}_i\Theta_i$. This can be demonstrated from (2.1) and (3.2). For clarity we momentarily ignore forcing and dissipation, obtaining

$$\begin{aligned}\frac{\partial\Theta_i}{\partial t} &= -\frac{H_i}{f_0}\left(\frac{\partial q_i}{\partial t} - \frac{\partial\,\nabla^2\psi_i}{\partial t}\right)\\ &= -\frac{H_i}{f_0}\left[-J(\psi_i, q_i) + J(\psi_i, \nabla^2\psi_i) - \frac{\mathrm{D}\,\nabla^2\psi_i}{\mathrm{D}t}\right]\\ &= -H_i\left[\frac{1}{f_0}J(\psi_i, \Theta_i) + \nabla\cdot\boldsymbol{u}_{a,i}\right],\end{aligned} \tag{3.3}$$

where $\mathrm{D}/\mathrm{D}t \equiv \partial/\partial t + J(\psi_i, \cdot)$, and $\boldsymbol{u}_{a,i}$ is the isallobaric ageostrophic velocity (e.g. Gill 1982, p. 498). Changes to Θ_i thus occur through advection by the geostrophic velocity, and through dilation arising from convergence of the ageostrophic velocity. Because the latter is excluded from the geostrophic velocity $\boldsymbol{u}$, averages of $\boldsymbol{u}_i\Theta_i$ will not correctly represent eddy fluxes of Θ_i.

To obtain an expression for eddy fluxes of Θ_i, we first express Θ_i in terms of q_i. From the Fourier transforms of (3.2) and (2.2)–(2.3),

$$\Theta_{1,\boldsymbol{k}} = \frac{H_1}{f_0}\frac{F_1}{k^2 + F_1 + F_2}(q_2 - h - q_1)_{\boldsymbol{k}}. \tag{3.4}$$

Thus, from the Fourier transform of (2.1),

$$\begin{aligned}\frac{\partial\Theta_{1,\boldsymbol{k}}}{\partial t} &= \frac{H_1}{f_0}\frac{F_1}{k^2 + F_1 + F_2}\left\{-J(\psi_2, q_2) + J(\psi_1, q_1) - D_2 + D_1 - \mathscr{F}\right\}_{\boldsymbol{k}}\\ &\equiv -\left\{\nabla\cdot[\boldsymbol{\Phi}_{\mathrm{adv}} + \boldsymbol{\Phi}_{\mathrm{dis}} + \boldsymbol{\Phi}_{\mathrm{for}}]\right\}_{\boldsymbol{k}},\end{aligned} \tag{3.5}$$

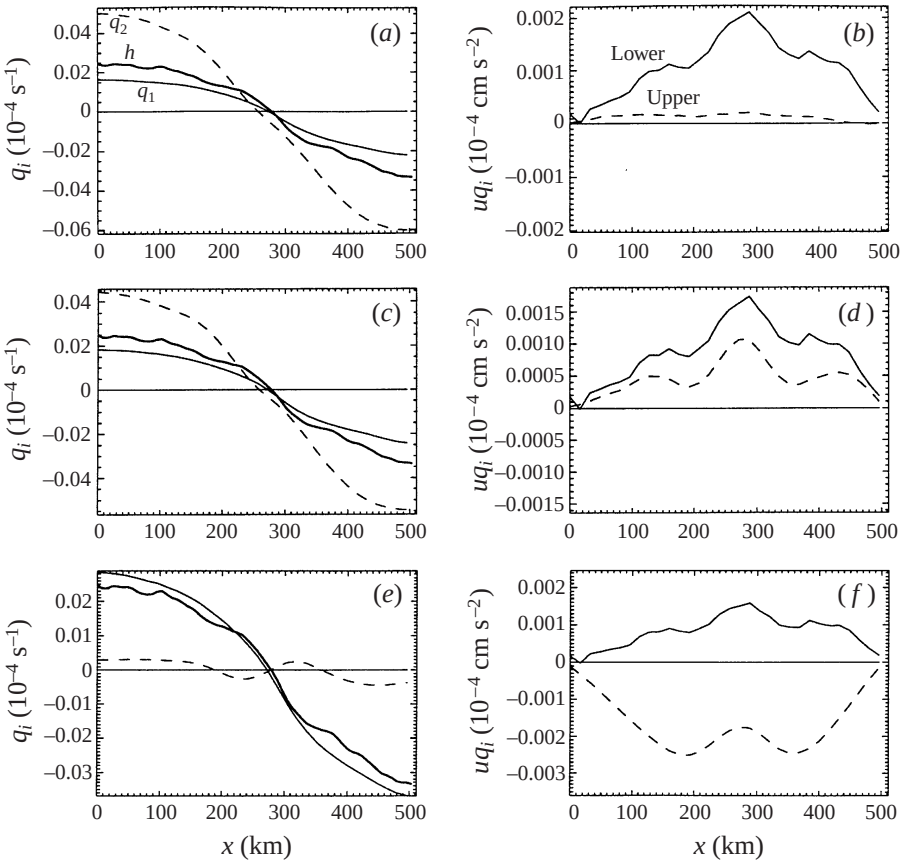

FIGURE 5. Temporal-mean potential vorticities q_i and eddy fluxes directed away from the ridge crest, vs. distance x from the ridge crest, for runs R2 (a, b), R2II (c, d), and R2III (e, f) having dissipation laws I, II and III. Quantities represent averages over y, on both sides of the ridge crest. Solid curves denote lower layer; dashed curves denote upper layer. In panels (a), (c) and (e), the averaged ridge profile h is indicated for reference by the thick curve.

where Φ_{adv}, Φ_{dis} and Φ_{for} denote layer thickness fluxes attributable to advection, dissipation and forcing. The advective contribution corresponds to the eddy flux discussed above.

We evaluate eddy fluxes of Θ_i from temporal means of $\nabla \cdot \Phi_{\mathrm{adv}}$ using Green's theorem. Mean fluxes away from the ridge axis, averaged in y, are given by

$$\langle \overline{\Phi}_{\mathrm{adv}} \rangle_x = \frac{1}{2L} \int_A \nabla \cdot \overline{\Phi}_{\mathrm{adv}} \, \mathrm{d}A, \tag{3.6}$$

where A denotes area within a distance x of the ridge axis. The dissipation and forcing contributions are evaluated similarly.

Figure 6 shows $\langle \overline{\Theta}_1 \rangle$ for run R2, along with the mean eddy and dissipative fluxes $\langle \overline{\Phi}_{\mathrm{adv}} \rangle_x$ and $\langle \overline{\Phi}_{\mathrm{dis}} \rangle_x$. (Because the y average of forcing is set to zero, the forcing contribution $\langle \overline{\Phi}_{\mathrm{for}} \rangle_x$ vanishes.) The eddy fluxes are countergradient and balance the downgradient dissipative fluxes, so that net flux vanishes in statistical equilibrium. Because $\Theta_2 = -\Theta_1$, eddy fluxes are countergradient in the lower layer as well. The other runs behave similarly.

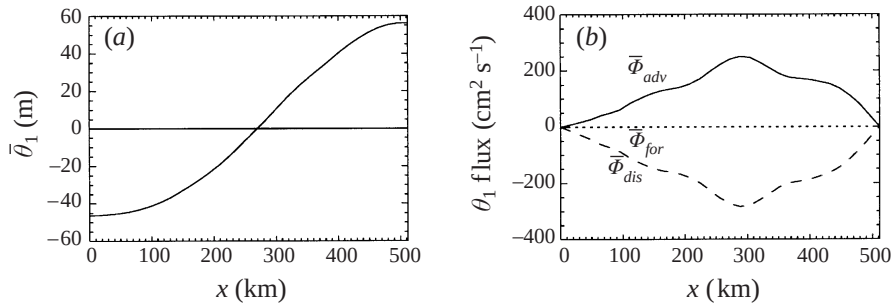

FIGURE 6. Temporally-averaged (*a*) layer thickness anomaly Θ_1, and (*b*) eddy fluxes of Θ_1 directed away from ridge crest, vs. distance x from the ridge crest, for run R2. Quantities represent averages over y, on both sides of the ridge crest. In (*b*), the solid curve indicates the eddy flux $\Phi_{\rm adv}$, and the dot-dashed curve the dissipative contribution $\Phi_{\rm dis}$. (The forcing contribution $\Phi_{\rm for}$ vanishes in this case.)

Quantity	R2bf	R3bf	R4bf	R5bf	R6bf	R2nr
L_D(km)	20	20	20	20	20	20
v_0 (s^{-1})	0.5×10^{-7}	1.6×10^{-7}	5×10^{-7}	1.6×10^{-6}	5×10^{-6}	0.5×10^{-7}
Dissipation law	I	I	I	I	I	I
$\langle u_1 \rangle$ (cm s^{-1})	20.6	14.3	10.0	8.3	11.3	6.4
$\langle u_2 \rangle$ (cm s^{-1})	21.6	14.8	9.1	4.4	1.7	3.1
$\langle \overline{u}_1 \rangle$ (cm s^{-1})	16.5	6.8	1.9	0.90	1.5	2.0
$\langle \overline{u}_2 \rangle$ (cm s^{-1})	17.3	7.7	2.6	0.71	0.16	1.7
$(\overline{C}_{\psi h})_1$	0.811	0.596	0.150	−0.151	−0.082	−0.642
$(\overline{C}_{\psi h})_2$	0.818	0.630	0.287	0.058	0.002	0.780
$\overline{A}_{\max} - \overline{A}_{\min}$ (m)	88	85	81	72	116	298
v_0/A	0.5	1.0	2.4	12	153	6.7
μ_1	0.34	1.5	2.0	6.2	8.5	67
μ_2	1.2	2.0	3.3	5.4	3.7	0.5

TABLE 3. Properties of barotropically-forced ridge runs R2bf–R6bf, run R2nr with no topographic roughness

3.4. *Barotropically forced runs*

To test whether the results described above are dependent upon the depth range of forcing, runs R2–R4 were repeated with forcing $\mathscr{F}$ applied identically in both layers, instead of in the upper layer alone (runs R2bf–R4bf; see table 3). In these runs, mean streamfunction is positively correlated with topography in both layers. However, when friction coefficient v_0 is increased further in runs R5bf and R6bf, offsetting the higher overall level of forcing, upper-layer mean flow reverses.

3.5. *Run with no topographic roughness*

Run R2nr is identical to run R2, except that we consider a smooth sinusoidal ridge having the same topographic variance as the bumpy ridge considered above. Minimum and maximum depths for the no-roughness topography are 4341 m and 4659 m. In this instance, lower-layer mean streamfunction again exhibits positive correlation with topography (table 3). However, upper-layer mean flow is reversed

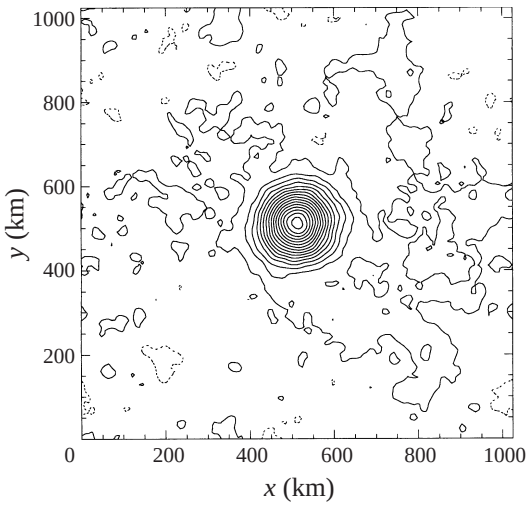

FIGURE 7. Seamount topography used in § 4. Solid contours denote regions above mean depth, and dashed contours regions below mean depth. Contour interval is 60 m.

Quantity	S1	S2	S3	S4
L_D (km)	5	20	20	20
ν_0 (s^{-1})	0.5×10^{-7}	0.5×10^{-7}	1.6×10^{-7}	5×10^{-7}
Dissipation law	I	I	I	I
$\langle u_1 \rangle$ (cm s^{-1})	5.5	11.6	11.7	9.5
$\langle u_2 \rangle$ (cm s^{-1})	5.3	6.0	3.6	1.9
$\langle \overline{u}_1 \rangle$ (cm s^{-1})	2.6	2.2	1.7	1.0
$\langle \overline{u}_2 \rangle$ (cm s^{-1})	2.7	2.8	1.1	0.38
$\overline{C}_{\psi h,1}$	0.337	0.168	−0.151	−0.101
$\overline{C}_{\psi h,2}$	0.350	0.347	0.151	0.045
$\overline{\Delta}_{\max} - \overline{\Delta}_{\min}$ (m)	116	125	221	136
ν_0/A	0.5	1.8	3.4	22

TABLE 4. Properties of seamount runs S2–S4 with upper-layer forcing

(streamfunction anticorrelated with topography) despite relatively small Rayleigh friction $\nu_0 = 0.5 \times 10^{-7}$ s^{-1}.

4. Seamount results

To assess further the generality of the results in § 3, particularly the tendency for upper-layer mean flow to reverse sign for sufficiently large ν_0, we consider runs S1–S4. These are identical to runs R1–R4, except that topography is a Gaussian seamount, with superposed roughness like that described in § 3 (figure 7). The seamount summit is 3338 m, and the maximum depth is 4611 m. The Gaussian half-width is 77 km. Properties of these solutions are described in table 4.

4.1. *Mean flows and interface deformations*

For run S2 with $\nu_0 = 0.5 \times 10^{-7}$ s^{-1}, mean streamfunction is similar to that of R2, i.e. anticyclonic over bumps and somewhat weaker in the upper layer (figure 8). For greater ν_0 (runs S3–S4), the solutions exhibit the same qualitative changes as R3–R4,

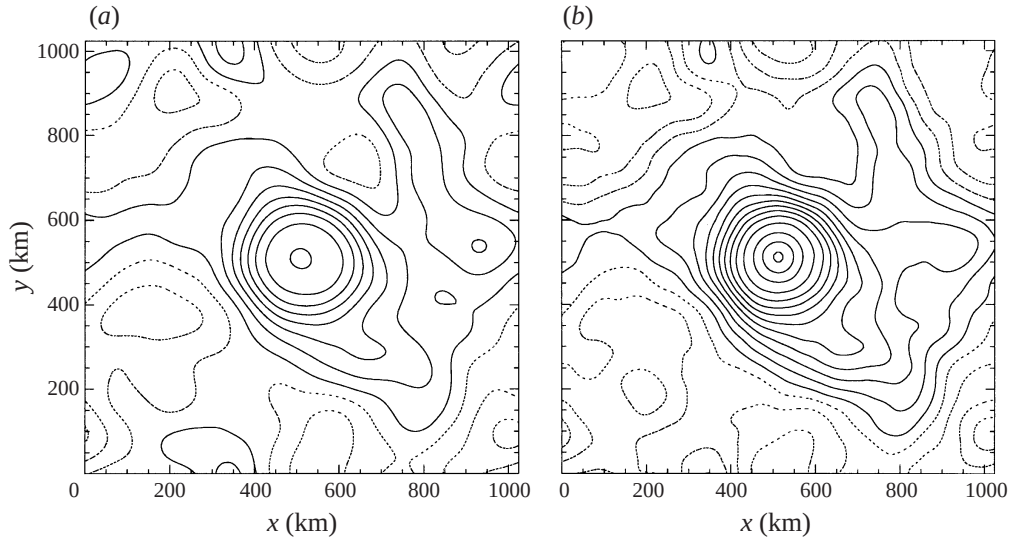

FIGURE 8. (*a*) Upper- and (*b*) lower-layer mean streamfunctions $\overline{\psi}_i$ for seamount run S2 having $v_0 = 0.5 \times 10^{-7}$ s^{-1}. Contour interval is 10^7 cm^2 s^{-1}. Solid contours are positive, and dashed contours negative.

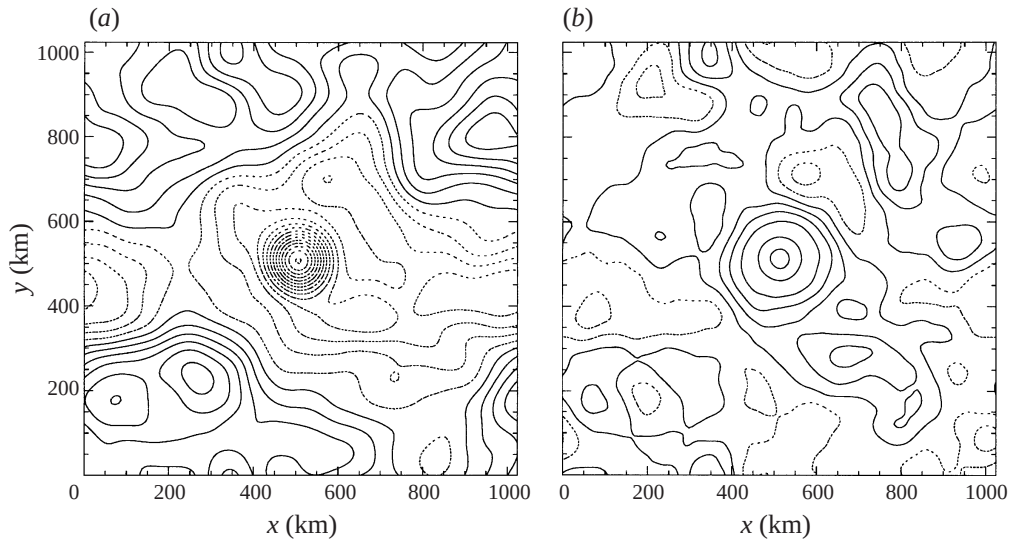

FIGURE 9. (*a*) Upper- and (*b*) lower-layer mean streamfunctions $\overline{\psi}_i$ for seamount run S3 having $v_0 = 1.6 \times 10^{-7}$ s^{-1}. Contour interval is 5×10^6 cm^2 s^{-1}. Solid contours are positive, and dashed contours negative.

i.e. reversed upper-layer mean flows which are stronger than those in the lower layer (figure 9). The interface between layers is domed over the seamount.

4.2. *Eddy fluxes of potential vorticity and layer thickness*

Potential vorticity and thickness fluxes for runs S1–S4 were evaluated as azimuthal averages of radial flux about the seamount summit, using procedures analogous to those described in § 3.2–§ 3.3. The fluxes are qualitatively similar to those of R1–R4,

with one exception: because azimuthal and temporal means of $\mathscr{F}$ do not identically vanish, the thickness flux contributions exhibit a three-way balance between eddy flux $\langle\overline{\Phi}_{\rm adv}\rangle_r$, dissipative flux $\langle\overline{\Phi}_{\rm dis}\rangle_r$, and the forcing contribution $\langle\overline{\Phi}_{\rm for}\rangle_r$.

5. Interpretation

In the model runs described above, forcing and dissipation balance the influence of eddies in statistical equilibrium. In this section, we develop a simple description for how this balance determines mean circulation and eddy fluxes.

5.1. *Mean flows*

In interpreting the above results, we consider forcing and dissipation as perturbing the flows from inviscid equilibria. Such equilibria possess maximum flow entropy (Carnevale, Frisch & Salmon 1981), and feature topographically-correlated mean streamfunctions, which can be found by statistical mechanics (Salmon *et al.* 1976). Forcing and dissipation draw such systems toward lower entropy (Zou & Holloway 1994; Merryfield & Holloway 1997). Eddies act oppositely, driving the flow toward higher entropy (Carnevale 1982; Zou & Holloway 1994).

In applying this principle to the results of § 3–§ 4, we suppose that the Jacobian terms in (2.1) draw the mean potential vorticities toward their maximum-entropy values $\overline{q}_i^*$. We attempt to treat these tendencies as simply as possible by replacing the mean Jacobian with $-A(q_i-\overline{q}_i^*)$, where A is a scale-dependent eddy relaxation timescale. Some motivation is provided by results of Merryfield & Holloway (1997), who investigated how inviscid equilibria of single-layer quasi-geostrophic models are perturbed by weak forcing. There it was argued that the tendency for eddies to maximize entropy gives rise to a restoring 'force' which grows linearly with (sufficiently small) departures from equilibrium. This tendency was demonstrated numerically by applying small torques to individual Fourier modes of vorticity, while keeping the system close to equilibrium with appropriately-chosen broadband dissipation. The resulting perturbations were proportional to the applied torques, with the largest effect on the Fourier mode being forced. Substituting $-A(q_i-\overline{q}_i^*)$ for the Jacobian terms in (2.1), Fourier transforming, ensemble averaging, selecting dissipation law I, and considering larger scales on which biharmonic friction is negligible yields

$$\frac{\partial\overline{q}_{1,\boldsymbol{k}}}{\partial t}=-A_{\boldsymbol{k}}(\overline{q}_{1,\boldsymbol{k}}-\overline{q}^*_{1,\boldsymbol{k}}), \tag{5.1a}$$

$$\frac{\partial\overline{q}_{2,\boldsymbol{k}}}{\partial t}=-A_{\boldsymbol{k}}(\overline{q}_{2,\boldsymbol{k}}-\overline{q}^*_{2,\boldsymbol{k}})+\nu_0k^2\overline{\psi}_{2,\boldsymbol{k}}. \tag{5.1b}$$

In statistical equilibrium, the temporal derivatives vanish, and mean circulation is determined by the eddy relaxation coefficients $A_{\boldsymbol{k}}$, the Rayleigh friction coefficient ν_0, and the maximum-entropy mean state $\overline{q}_i^*$. Using (2.2)–(2.3), we estimate $\overline{q}_i^*$ from the maximum-entropy mean streamfunctions of Salmon *et al.* (1976), which can be written

$$\overline{\psi}^*_{1,\boldsymbol{k}}=\frac{F_1h_{\boldsymbol{k}}}{\Lambda},\quad \overline{\psi}^*_{2,\boldsymbol{k}}=\frac{(k^2+F_1+\mu_1)h_{\boldsymbol{k}}}{\Lambda}, \tag{5.2}$$

where

$$\Lambda\equiv k^2(k^2+F_1+F_2)+\mu_1(k^2+F_2)+\mu_2(k^2+F_1)+\mu_1\mu_2. \tag{5.3}$$

Here, $\mu_i\equiv\alpha/\beta_i$, $i=1,2$, where α and β_i are Lagrange multipliers determined by total energy and potential enstrophy in the two layers.

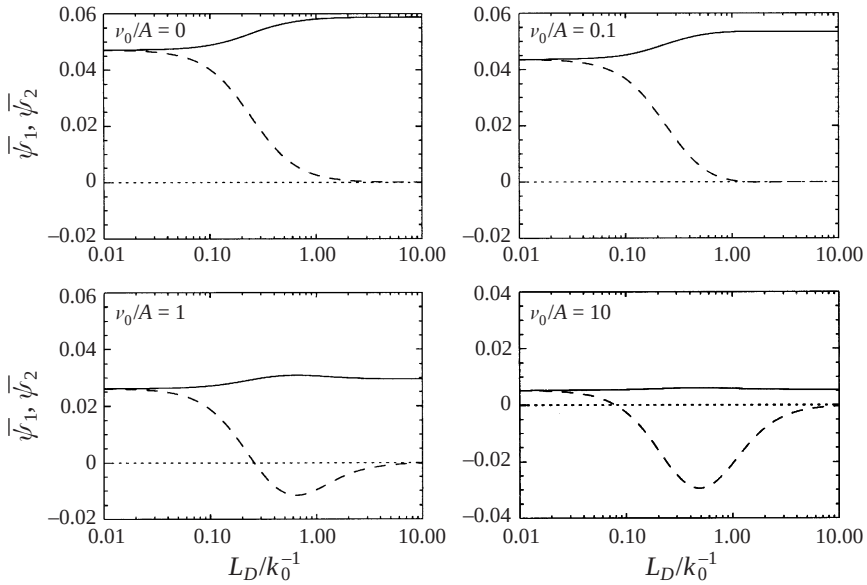

FIGURE 10. Predicted mean streamfunctions $\overline{\psi}_{i,\boldsymbol{k}}$ (for unit $h_{\boldsymbol{k}}$), as functions of L_D and ratio v_0/A of damping to eddy relaxation timescales, from equations (A 3)–(A 4). Solid curves denote lower layer; dashed curves denote upper layer. In each panel $k = k_0$ and $\mu_1 = \mu_2 = 16k_0^2$.

Substituting (5.2)–(5.3) into (5.1) yields expressions for perturbed $\overline{\psi}_{i,\boldsymbol{k}}$ and mean interface displacement $\overline{\Delta}_{\boldsymbol{k}}$, as detailed in the Appendix. The results depend mainly on deformation radius $L_D = (H_1H_2/H_0^2F)^{1/2}$ and the ratio $v_0/A_{\boldsymbol{k}}$. Figure 10 shows $\overline{\psi}_{1,\boldsymbol{k}}$ and $\overline{\psi}_{2,\boldsymbol{k}}$ as functions of L_D for $k = k_0$ and selected values of $v_0/A_{\boldsymbol{k}}$, for particular choices of μ_1 and μ_2. For $v_0/A_{\boldsymbol{k}} = 0$, we recover the inviscid results (5.2)–(5.3), which feature substantial attenuation of $\overline{\psi}_{1,\boldsymbol{k}}$ when $L_D \gtrsim k_0^{-1}$. For $v_0/A_{\boldsymbol{k}} = 0.1$, the results are much the same. However, for $v_0/A_{\boldsymbol{k}} \gtrsim 1$, pronounced changes occur. In the bottom layer, $\overline{\psi}_{2,\boldsymbol{k}}$ suffers significant damping, as one might expect. In the top layer, $\overline{\psi}_{1,\boldsymbol{k}}$ reverses sign when L_D becomes an appreciable fraction of k_0^{-1}. For $v_0/A_{\boldsymbol{k}} \gg 1$, the reversed upper-layer mean flow can exceed the lower-layer mean flow in strength.

From (A 3)–(A 5), one can show that for arbitrary fixed k, F_i and $\mu_i > 0$, $\overline{\psi}_{i,\boldsymbol{k}}$ and $\overline{\Delta}_{\boldsymbol{k}}$ monotonically decrease with increasing $v_0/A_{\boldsymbol{k}}$, with bounds

$$\underline{v_0/A_{\boldsymbol{k}} = 0} \quad \underline{v_0/A_{\boldsymbol{k}} \to \infty}$$

$$\overline{\psi}^*_{1,\boldsymbol{k}} \geqslant \overline{\psi}_{1,\boldsymbol{k}} > \frac{-\mu_1}{k^2 + F_1}\overline{\psi}^*_{1,\boldsymbol{k}}, \tag{5.4a}$$

$$\overline{\psi}^*_{2,\boldsymbol{k}} \geqslant \overline{\psi}_{2,\boldsymbol{k}} > 0, \tag{5.4b}$$

$$\overline{\Delta}^*_{\boldsymbol{k}} \geqslant \overline{\Delta}_{\boldsymbol{k}} > \frac{\mu_1 F_1}{(k^2 + \mu_1)(k^2 + F_1)}\overline{\Delta}^*_{\boldsymbol{k}}. \tag{5.4c}$$

We interpret these results as follows. As v_0 increases, $\overline{\psi}_{2,\boldsymbol{k}}$ becomes increasingly damped. This reduces $|\overline{\psi}_{2,\boldsymbol{k}} - \overline{\psi}_{1,\boldsymbol{k}}|$, and hence the height of interfacial domes. In the upper layer, $\overline{q}_{1,\boldsymbol{k}}$ experiences no appreciable damping on the scales considered, so that $\overline{q}_{1,\boldsymbol{k}} = \overline{q}^*_{1,\boldsymbol{k}}$ from (5.1a). But $\overline{q}_{1,\boldsymbol{k}}$ is the sum of mean relative vorticity (negative for positive $\overline{\psi}_{1,\boldsymbol{k}}$) and planetary vorticity arising from deformation of the interface. The latter is smaller than at maximum entropy due to the reduced interfacial dome height. Relative vorticity $-k^2\overline{\psi}_{1,\boldsymbol{k}}$ therefore must be larger than at maximum entropy,

implying reduced $\overline{\psi}_{1,\boldsymbol{k}}$. If Rayleigh friction reduces the interfacial displacement more than $(k^2H_0/f_0)\overline{\psi}^*_{1,\boldsymbol{k}}$, the sign of $\overline{\psi}_{1,\boldsymbol{k}}$ reverses.

The numerical results of § 3–§ 4 exhibit trends similar to those just described: $\overline{\psi}_1$ decreases as L_D increases, and changes sign if ν_0 is sufficiently large. Also, $\overline{\Delta}$ always is domed over topographic elevations. To enable direct comparisons between the numerical solutions and solutions to (5.1), we estimate the restoring coefficients A, ignoring dependence on wavenumber, as follows. First, the model runs are resumed with forcing and dissipation absent. (Residual numerical dissipation is insignificant on timescales of interest.) The streamfunction–topography correlations $C_{\psi h,i}$, as well as other model parameters, then relax toward maximum-entropy values. Following least-squares fits of $C_{\psi h,i}(t)$ to exponential decay laws, approximate values for A are inferred from means of the best-fit exponential decay rates in the two layers. Values of ν_0/A for each run are indicated in tables 2–4.

The reason for upper-layer mean flow reversal in the smooth-ridge run R2nr despite relatively small $\nu_0 = 0.5 \times 10^7$ s^{-1} now becomes clear. In this run, the absence of topographic roughness leads to an order-of-magnitude reduction in eddy relaxation rate A. (Such an effect was noted also in barotropic simulations by Cummins & Holloway 1994.) This results in relatively large $\nu_0/A = 6.7$, promoting flow reversal as discussed above.

Figure 11 provides a comparison of predicted vs. numerical-model values for the Fourier component of the mean streamfunction corresponding to the ridge. The labelled plus signs, denoting the forced-dissipative runs with ridge topography and dissipation law I, are connected by solid lines to asterisks denoting the corresponding (equilibrated) inviscid runs. To obtain predicted $\overline{\psi}$, equations (5.2)–(5.3) and (A 2)–(A 3) were evaluated using values for μ_1 and μ_2 deduced from the inviscid runs. Because the Fourier transforms of (5.2), (5.3) are equivalent to $\mu_i\overline{\psi}^*_i = \overline{q}^*_i$, $i = 1, 2$ (Merryfield 1998), one can find μ_i from the slopes defined by scatter plots of $\overline{\psi}^*_i$ vs. $\overline{q}^*_i$ in instances where (5.2)–(5.3) hold. These relations are formally valid only for random initial conditions and topography. However, we found that for bumpy ridge topography, the $\overline{\psi}^*_i$–$\overline{q}^*_i$ relations are very nearly linear, even though the topography contains a significant non-random feature. In such instances, the μ_i could be estimated from linear least-squares fits. In the case of the smooth ridge (run R2nr), the $\overline{\psi}^*_i - \overline{q}^*_i$ relation was significantly nonlinear. (This may in part be due to the very slow equilibration of the inviscid run.) In this instance, approximate values for μ_i were determined from $\mu_i \approx \Delta\overline{q}^*_i/\Delta\overline{\psi}^*_i$, where $\Delta\overline{q}^*_i$ and $\Delta\overline{\psi}^*_i$ denote differences between extrema of $\overline{q}^*_i$ and $\overline{\psi}^*_i$. We did not attempt such determinations for the seamount runs, for which the $\overline{\psi}^*_i - \overline{q}^*_i$ relations are markedly nonlinear. In Figure 11, the ability of (A 3)–(A 4) to represent numerical model behaviour is indicated by proximity of the symbols to unit slope (dashed line). The predictions appear reasonable with respect to the magnitude of inviscid equilibrium mean flows, and to their modification by Rayleigh friction. In particular, (A 3) provides reasonably accurate indications of when the upper-layer mean flow reverses sense.

Equation (A 3) also predicts that numerical solutions which exhibit negative $\overline{\psi}_1$–h correlation on large scales should exhibit positive $\overline{\psi}_1$–h correlation on sufficiently small scales. Such a reversal is seen in all runs for which large-scale $\overline{\psi}_1$–h correlation is negative, occurring between $k = 2k_0$ and $6k_0$. Figure 12 shows $\overline{\psi}_{i,\boldsymbol{k}}$ for unit $h_{\boldsymbol{k}}$ as functions of k, averaged in bins of unit k, for run R4. Lower-layer $\overline{\psi}_{2,\boldsymbol{k}}$ (•) is positive for all k, whereas $\overline{\psi}_{1,\boldsymbol{k}}$ (○) reverses from negative to positive at $k \approx 6k_0$. The thin curves plot (A 3) and (A 4), for constant $A_{\boldsymbol{k}} = 1.25 \times 10^{-7}$ s^{-1} and with $\mu_1 = 17k_0^2$,

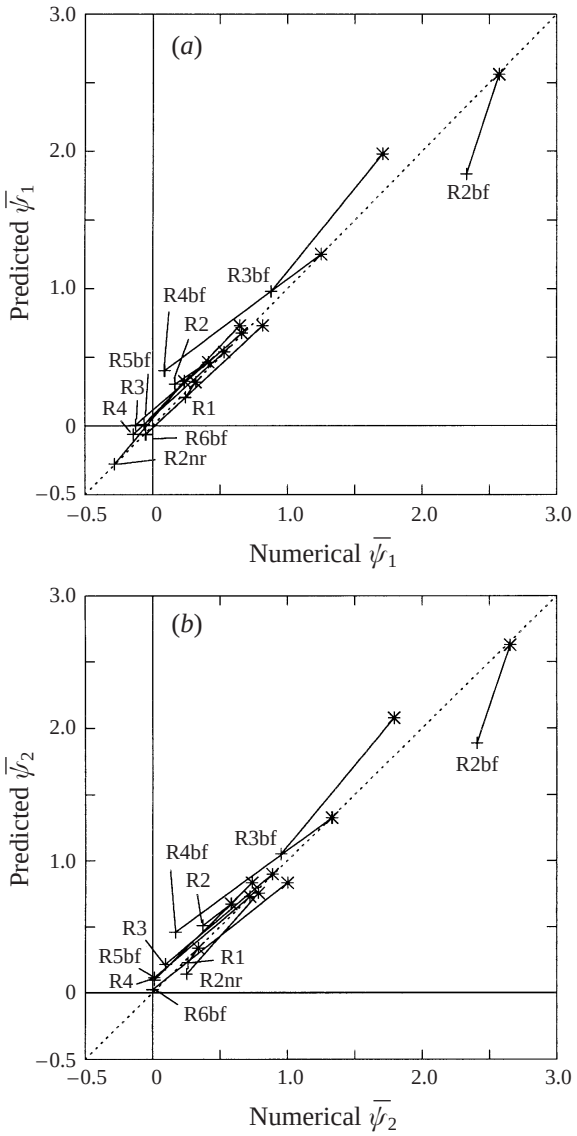

FIGURE 11. Comparison of predicted mean streamfunctions $\overline{\psi}_{i,\boldsymbol{k}}$ corresponding to ridge with those found numerically, for ridge runs with dissipation law I. Plus signs denoting forced-dissipative runs are joined by solid lines to asterisks denoting inviscid counterparts. Dashed lines of unit slope indicate perfect prediction. (*a*) Upper layer, (*b*) lower layer.

$\mu_2 = 4.8k_0^2$, values characterizing the inviscid continuation of R4. For the thick curves, $A_{\boldsymbol{k}} = 6.25 \times 10^{-9}(k/k_0)^2$ s^{-1}. The superiority of the latter fit suggests that $A_{\boldsymbol{k}}$, and hence the rate at which eddies drive the flow toward higher entropy, increases toward smaller scales. The extent to which this tendency may depend upon statistics of the topography and flow remains to be explored.

5.2. *Eddy fluxes of potential vorticity*

In § 3.2, largest-scale eddy fluxes of potential vorticity in the lower layer were found to be downgradient. Those in the upper layer were nearly vanishing, downgradient,

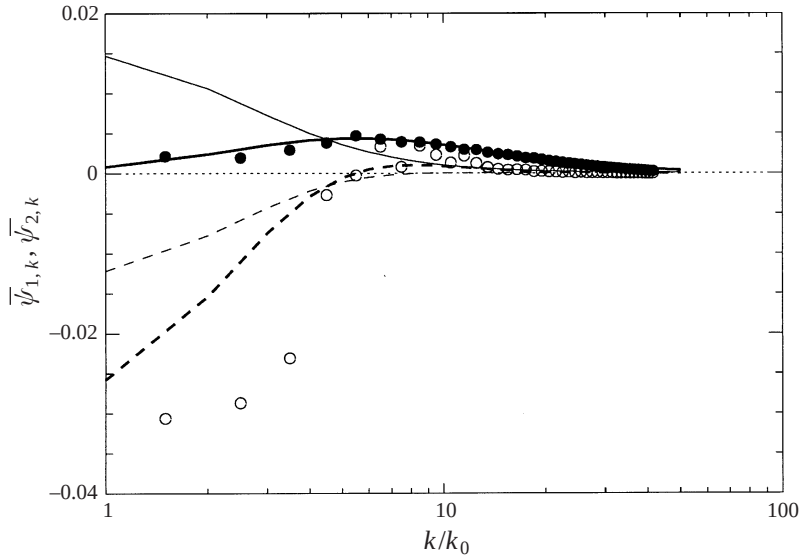

FIGURE 12. Mean streamfunctions $\overline{\psi}_{i,k}$ (for unit h_k), as functions of k, for run R4 having $\nu_0 = 5 \times 10^{-7}$ s^{-1}; ○, upper-layer values; •, lower-layer values. The thin curves plot equations (A 3)–(A 4) with $A_k = 6.25 \times 10^{-8}$ s^{-1} and $\mu_1 = 17k_0^2$, $\mu_2 = 4.8k_0^2$ characterizing run R4 when forcing and dissipation are turned off. The thick curves are similar, but with $A_k = 3.12 \times 10^{-9}(k/k_0)^2$ s^{-1}. Solid curves denote lower layer; dashed curves denote upper layer.

or countergradient for dissipation laws I, II and III. Here we interpret this behaviour in terms of the tendency for eddies to drive the flow toward higher entropy.

In the absence of mean forcing, mean eddy fluxes of potential vorticity must balance dissipation in statistical equilibrium. For dissipation law I, upper-layer dissipation on the largest scales is extremely small, and so the opposing eddy fluxes nearly vanish. For law II, upper-layer dissipation acts upon relative vorticity, which is negative over topographic elevations. This tends to build up the positive potential vorticity anomaly. The opposing eddy fluxes must reduce positive $\overline{q}_1$, and therefore are downgradient. For law III, dissipation reduces the positive anomalies of $\overline{q}_1$ found over topographic elevations. The opposing eddy fluxes build up positive anomalies of $\overline{q}_1$, and therefore are countergradient.

In the lower layer, dissipation acts upon relative vorticity, which again is negative over topographic elevations. This tends to increase the positive potential vorticity $\overline{q}_2$. The opposing eddy fluxes tend to reduce $\overline{q}_2$, and therefore are downgradient.

In each instance, the eddy fluxes tend to relax $\overline{q}_i$ not toward homogeneity, but toward the maximum-entropy values $\overline{q}_i^*$ which occur when forcing and dissipation are absent. The eddy fluxes thus are consistently downgradient with respect to $\overline{q}_i - \overline{q}_i^*$.

5.3. *Eddy fluxes of layer thickness*

In § 3.3 and § 4.2, fluxes of layer thickness anomaly Θ_i on the largest scales were found to be countergradient in both layers. This behaviour can be understood as follows. For dissipation law I, dissipation on large scales acts almost entirely in the lower layer. Because dissipation damps large-scale $\overline{\psi}_2$ but not $\overline{\psi}_1$, the interfacial deformation, proportional to $|\overline{\psi}_2 - \overline{\psi}_1|$, is reduced. The opposing influence of eddies builds up interfacial deformation, driving Θ_i away from $\overline{\Theta}_i = 0$ and toward $\overline{\Theta}_i = \overline{\Theta}_i^*$. Eddy

fluxes thus are countergradient with respect to $\overline{\Theta}_i$, but downgradient with respect to $\overline{\Theta}_i - \overline{\Theta}_i^*$.

6. Implications for eddy parameterizations

In §3–§5 we showed that eddy fluxes of layer thickness, potential vorticity and momentum tend to drive the mean states of stratified quasi-geostrophic models toward higher entropy. In this section, we consider how these results bear upon various eddy parameterizations.

6.1. *Parameterizations of eddy thickness flux*

One class of eddy parameterizations assumes that available potential energy of the large-scale flow is released by eddy-generating baroclinic instabilities, leading to flattening of isopycnal surfaces. Such parameterizations have been formulated for level (Gent & McWilliams 1990; Gent *et al.* 1995; Visbeck, *et al.* 1997) and layer (McCreary & Kundu 1988; Cherniawsky & Holloway 1991; Bleck *et al.* 1992) models, as discussed further by Holloway (1997). The parameterization of Gent & McWilliams (1990; see also Gent *et al.* 1995), for example, relaxes isopycnals by imposing nearly-Fickian down-gradient diffusion of layer thickness. The Gent & McWilliams parameterization leads to apparent improvements ocean circulation models (e.g. Danabasoglu & McWilliams 1995).

The supposition that eddies lead strictly to down-gradient thickness diffusion conflicts with the numerical results of §3–§4. Especially, we observe upper-layer thickness fluxes which build and sustain isolated thickness extrema, contrary to down-gradient diffusion. When topography is present, eddies tend to drive mean isopycnals toward shapes which reflect bathymetry, affecting thickness anomalies throughout the water column.

To account for the tendency for eddies to drive the system toward higher entropy, thickness diffusion parameterizations should diffuse thickness anomaly not toward $\Theta = 0$, but toward a higher-entropy, topographically-correlated Θ^*, whose specification is discussed in §6.4. Eddy thickness flux is then proportional to $\nabla(\Theta - \Theta^*)$. One consequence of this approach is that when eddy thickness fluxes at a particular location are persistently countergradient, as in the examples of §3–§4, eddy tracer fluxes also are countergradient. Such a tendency has been observed at Fieberling Guyot, where radial eddy heat transport *lowers* temperature in the overlying cold dome (Brink 1995).

6.2. *Parameterizations of eddy potential vorticity flux*

Another class of eddy parameterizations assumes down-gradient lateral diffusion of potential vorticity (e.g. Marshall 1981; Rhines & Young 1982; Thompson 1995; Treguier, Held & Larichev 1997). Such eddy fluxes are equivalent to vertical transport of momentum by interfacial form drag (Greatbach & Lamb 1990). By considerations similar to those in §6.1, diffusion of q down gradients of $\nabla(q - q^*)$ may represent eddy potential vorticity fluxes more accurately than diffusion down gradients of q.

6.3. *Parameterizations of eddy momentum flux*

A consequence of eddies driving flows toward higher entropy is the generation of topographically-correlated currents which are anticyclonic over bumps (Haidvogel & Brink 1986; Holloway 1987; Treguier 1989; Merryfield & Holloway 1997). To parameterize this effect, Holloway (1992) suggested replacing the usual eddy viscosity, which

relaxes horizontal velocity $\boldsymbol{u}$ toward rest, by a term which relaxes $\boldsymbol{u}$ towards a higher-entropy mean flow $\boldsymbol{u}^*$. Specification of $\boldsymbol{u}^*$ was drawn from the Salmon *et al.* (1976) description of the maximum-entropy states of unstratified quasi-geostrophic models. This particularly simple form for $\boldsymbol{u}^*$ has been employed in several ocean circulation studies, with apparent improvements in model fidelity (Alvarez, *et al.* 1994; Eby & Holloway 1994; Fyfe & Marinone 1995; Sou, Holloway & Eby 1995; Pal & Holloway 1996; Nazarenko *et al.* 1997). An alternative specification for $\boldsymbol{u}^*$ which accounts for stratification is discussed below.

6.4. *Specification of Θ^*, q^*, $\boldsymbol{u}^*$*

Sections 6.1–6.3 discussed parameterizations of the tendency for eddies to drive the flow toward higher entropy. Here we consider how to specify the high-entropy thickness Θ^*, potential vorticity q^*, and horizontal velocity $\boldsymbol{u}^*$, drawing upon analytical results for continuously stratified quasi-geostrophic models (Merryfield 1998). For especially simple illustration, we consider the case of uniform stratification.

For uniform Brunt–Väisälä frequency N, the Fourier components of the maximum-entropy mean streamfunction are

$$\overline{\psi}^*_{\boldsymbol{k}}(z) = \frac{h_{\boldsymbol{k}}}{\mu + k^2} K H_0 \frac{\cosh Kz}{\sinh KH_0}, \tag{6.1}$$

where

$$K \equiv \frac{N}{f_0}(\mu + k^2)^{1/2} = \frac{L_D}{H_0}(\mu + k^2)^{1/2}. \tag{6.2}$$

The function $\mu(z)$, determined by total energy and potential enstrophy as a function of depth, is here assumed uniform.

The maximum-entropy mean isopycnal deformations, given by

$$\begin{aligned} \overline{\Delta}^*_{\boldsymbol{k}} &= \frac{f_0}{N^2}\frac{\mathrm{d}\psi^*_{\boldsymbol{k}}}{\mathrm{d}z} \\ &= \frac{h_{\boldsymbol{k}}}{f_0} H_0 \frac{\sinh Kz}{\sinh KH_0}, \end{aligned} \tag{6.3}$$

describe domes over elevated topography. The corresponding thickness anomalies are

$$\begin{aligned} \overline{\Theta}^*_{\boldsymbol{k}} = -\frac{\mathrm{d}}{\mathrm{d}z}\overline{\Delta}^*_{\boldsymbol{k}} &= -\frac{1}{f_0}\left[k^2 + \mu\right]\overline{\psi}^*_{\boldsymbol{k}} \\ &= -\frac{h_{\boldsymbol{k}}}{f_0} K H_0 \frac{\cosh Kz}{\sinh KH_0}, \end{aligned} \tag{6.4}$$

so that thickness anomalies over elevated topography are negative.

The equilibrium mean potential vorticity is related to mean streamfunction by

$$\overline{q}^*_{\boldsymbol{k}}(z) = \mu \overline{\psi}^*_{\boldsymbol{k}}(z), \tag{6.5}$$

and the horizontal velocity $\overline{\boldsymbol{u}}^* = (\overline{u}^*, \overline{v}^*)$ can be determined from

$$\overline{u}^* = -\frac{\partial \overline{\psi}^*}{\partial y}, \quad \overline{v}^* = \frac{\partial \overline{\psi}^*}{\partial x}. \tag{6.6}$$

These solutions depend strongly upon stratification. When $KH_0 \ll 1$, effects of stratification are weak, and the mean streamfunction (6.1)–(6.2) becomes nearly barotropic. Isopycnal deformation increases linearly with depth, and $\overline{\Theta}^*(z)$ becomes depth-independent. Stratification effects become important when $KH_0 \gtrsim 1$, which

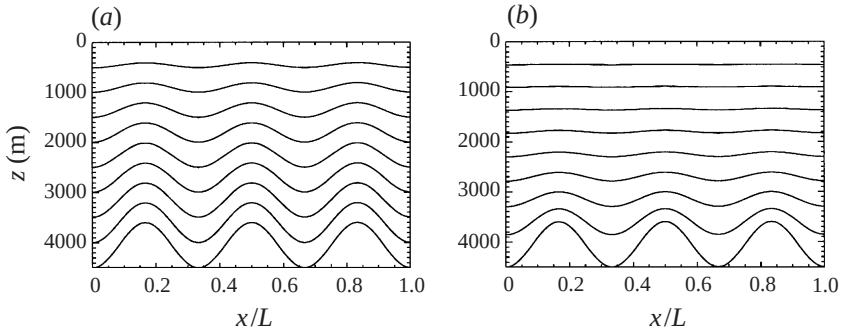

FIGURE 13. Mean isopycnals for maximum-entropy flow over a sinusoidal ridge, for uniform continuous stratification. (*a*) Weak stratification ($KH_0 = 0.5$). (*b*) Strong stratification ($KH_0 = 5$).

occurs (i) on spatial scales smaller than L_D, or (ii) on *all* spatial scales, provided that $\mu^{-1/2} \gtrsim L_D$. The mean flow then becomes increasingly bottom-trapped, with scale height K^{-1}. Isopycnal deformations and thickness anomalies are confined within a distance K^{-1} of the bottom. Figure 13 shows mean isopycnals for maximum-entropy flow above a sinusoidal ridge, for $KH_0 = 0.5$ and $KH_0 = 5$.

Application to realistic ocean models having lateral boundaries is greatly simplified if model resolution is coarser than the lengthscale $\mu^{-1/2}$. Then q^*, $\boldsymbol{\Theta}^*$ and $\boldsymbol{u}^*$ can be determined from $\overline{\psi}_i^*$ through an ordinary differential equation

$$\frac{\mathrm{d}}{\mathrm{d}z}\left[\frac{f_0^2}{N^2(z)}\frac{\mathrm{d}\overline{\psi}^*}{\mathrm{d}z}\right] - \mu\overline{\psi}^*(z) = 0, \tag{6.7}$$

solved at each horizontal grid location (Merryfield 1998). The magnitude of $\mu^{-1/2}$ has been related to eddy lengthscales (Holloway 1992), although a more confident prescription for μ would be desirable. As a further refinement one could consider the z-dependence of μ; additional work is needed to establish such a choice.

7. Discussion

Some of the properties described above have been observed in other contexts, most notably in studies of tidal rectification by banks and seamounts. Anticyclonic mean flows above topographic elevations have been seen in the laboratory experiments of Zhang & Boyer (1993) and Codiga (1993) and the primitive-equation numerical models of Chen & Beardsley (1995) and Beckmann & Haidvogel (1997). In the latter model the anticyclonic vortex is capped by a reverse (cyclonic) circulation which qualitatively resembles the reversed upper-layer mean flows described here. The tidal rectification models exhibit isopycnal doming over summits.

Care must be taken in making such comparisons because of differences between primitive-equation models and a quasi-geostrophic model. For example, the primitive equation models support mixing in the benthic boundary layer, which deflects isopycnals bottomward. The resulting radial pressure gradient drives an upslope cyclonic flow in the bottom boundary layer and a downslope, anticyclonic flow which dominates azimuthal transport above (Cummins & Foreman 1998 and references therein). This tendency can contribute to mean-flow generation in tidal rectification models.

Other phenomena bearing on vorticity production over topography include Taylor caps (Chapman & Haidvogel 1992), trapped waves (Haidvogel *et al.* 1993), and vortex shedding (Smith 1992; Schär & Smith 1993). As well, baroclinic instability

generates eddies when the bottom is flat. Such processes provide pathways, generating fluctuations and yielding higher entropy. Statistical-mechanics-based descriptions are essentially amechanistic in that details of processes effecting higher entropy are not considered, much as collisions in a gas effect relaxation toward equilibrium without requiring detailed consideration of the collisions themselves.

The principles considered here can be invoked even when topography plays no role. For example, in the case of wind-driven circulation in a flat-bottomed channel (e.g. Visbeck *et al.* 1997), our formulation would treat eddies as relaxing mean potential vorticity toward $q^* = 0$. An alternative formulation described by Kazantsev, Sommeria & Verron (1998) uses statistical mechanics to parameterize eddies in a barotropic, flat-bottomed basin. Their scheme stipulates that fluxes due to unresolved motions act to maximize the rate of entropy production, as deduced from the statistical theory of Robert & Sommeria (1991, 1992). Such a procedure can also be applied with arbitrary (non-random) topography.

8. Conclusions

We have sought to characterize eddy transports when topography and stratification are important. Eddy effects were illustrated numerically in two-layer models of randomly forced flow over ridge and seamount topographies in which the dissipation law, depth dependence of random forcing, and degree of stratification were varied. All numerical solutions exhibited isopycnal doming and anticyclonic mean flow over topographic elevations in the lower layer. The sense of upper-layer mean flow can reverse when lower-layer Rayleigh friction is sufficiently large. Radial eddy fluxes of layer thickness anomaly are countergradient. Fluxes of potential vorticity anomaly are downgradient in the lower layer, and nearly vanishing, downgradient, or countergradient in the upper layer, depending upon the choice of upper-layer dissipation law. These tendencies are consistent with eddies driving the system toward higher-entropy states, rather than toward rest. A simple description in which dissipation balances the entropy generation tendency of eddies yields predictions consistent with the numerical results.

We suggest that eddy parameterizations can be improved by accounting for such behaviour. For example, parameterizations for eddy fluxes of potential vorticity and layer thickness should diffuse these quantities not down gradients of q and Θ, but down gradients of $q - q^*$ and $\Theta - \Theta^*$, where q^* and Θ^* are high-entropy states which can be estimated from the maximum-entropy equilibria of quasi-geostrophic models. We also suggest that a parameterization for eddy fluxes of momentum could be improved by choosing bottom-intensified $\boldsymbol{u}^*$, rather than the barotropic form used previously.

This work was supported by the Office of Naval Research (N00014-96-I-0518), and by a Fellowship to W.J.M. from the NOAA Postdoctoral Program in Climate and Global Change. The paper benefited from the thoughtful comments of three anonymous referees.

Appendix. Equilibrium solutions of (5.1)

Equilibrium solutions of equations (5.1) for $\overline{\psi}_{i,\boldsymbol{k}}$ and $\overline{A}_{\boldsymbol{k}}$ are obtained by substituting for $\overline{q}_{i,\boldsymbol{k}}$ from (2.2)–(2.3), and specifying $\overline{\psi}^*_{i,\boldsymbol{k}}$ from (5.2)–(5.3), yielding

$$-(k^2 + F_1)\overline{\psi}_{1,\boldsymbol{k}} + F_1\overline{\psi}_{2,\boldsymbol{k}} = \mu_1\overline{\psi}^*_{1,\boldsymbol{k}}, \tag{A 1}$$

$$F_2\overline{\psi}_{1,\boldsymbol{k}} - \left[(k^2 + F_2) + \frac{\nu_0}{A}k^2\right]\overline{\psi}_{2,\boldsymbol{k}} = \mu_2\overline{\psi}^*_{2,\boldsymbol{k}} - h_{\boldsymbol{k}}. \tag{A 2}$$

The solution can be written

$$\overline{\psi}_{1,\boldsymbol{k}} = \frac{1 - \dfrac{\nu_0}{A}\dfrac{\mu_1}{k^2 + F_1 + F_2}}{1 + \dfrac{\nu_0}{A}\dfrac{k^2 + F_1}{k^2 + F_1 + F_2}}\overline{\psi}^*_{1,\boldsymbol{k}}, \tag{A 3}$$

$$\overline{\psi}_{2,\boldsymbol{k}} = \frac{1}{1 + \dfrac{\nu_0}{A}\dfrac{k^2 + F_1}{k^2 + F_1 + F_2}}\overline{\psi}^*_{2,\boldsymbol{k}}. \tag{A 4}$$

From these results, together with (4.4),

$$\overline{\Delta}_{\boldsymbol{k}} = \frac{1 + \dfrac{\nu_0}{A}\dfrac{\mu_1 F_1}{(k^2 + F_1 + F_2)(k^2 + \mu_1)}}{1 + \dfrac{\nu_0}{A}\dfrac{k^2 + F_1}{k^2 + F_1 + F_2}}\overline{\Delta}^*_{\boldsymbol{k}}. \tag{A 5}$$

REFERENCES

Alvarez, A., Tintore, J., Holloway, G., Eby, M. & Beckers, J. M. 1994 Effect of topographic stress on the circulation in the western Mediterranean. *J. Geophys. Res.* **99**, 16053–16064.

Beckmann, A. & Haidvogel, D. B. 1997 A numerical simulation of flow at Fieberling Guyot. *J. Geophys. Res.* **102**, 5595–5613.

Bleck, R., Rooth, C., Hu, D. & Smith, L. T. 1992 Salinity-driven thermohaline transients in a wind- and thermohaline-forced isopycnic coordinate model of the North Atlantic. *J. Phys. Oceanogr.* **22**, 1486–1515.

Brink, K. H. 1995 Tidal and lower frequency currents above Fieberling Guyot. *J. Geophys. Res.* **100**, 10817–10832.

Canuto, C., Hussaini, M. Y., Quarteroni, A. & Zang, T. A. 1988 *Spectral Methods in Fluid Mechanics.* Springer.

Carnevale, G. F. 1982 Statistical features of the evolution of two-dimensional turbulence *J. Fluid Mech.* **122**, 143–153.

Carnevale, G. F., Frisch, U. & Salmon, R. 1981 *H* theorems in statistical fluid dynamics. *J. Phys.* A **14**, 1701–1718.

Chapman, D. C. & Haidvogel, D. B. 1992 Formation of Taylor caps over a tall isolated seamount in a stratified ocean. *Geophys. Astrophys. Fluid Dyn.* **64**, 31–65.

Chen, C. & Beardsley, R. C. 1995 A numerical study of tidal rectification over finite-amplitude banks. Part I: Symmetric Banks. *J. Phys. Oceanogr.* **25**, 2090–2109.

Cherniawsky, J. & Holloway, G. 1991 An upper ocean general circulation model for the North Pacific: Preliminary experiments. *Atmos. Ocean* **29**, 737–784.

Codiga, D. L. 1993 Laboratory realizations of stratified seamount-trapped waves. *J. Phys. Oceanogr.* **23**, 2053–2071.

Cummins, P. F. & Foreman, M. G. G. 1998 A numerical study of circulation driven by mixing over a submarine bank. *Deep-Sea Res.* **45**, 745–769.

Cummins, P. F. & Holloway, G. 1994 On eddy-topographic stress representation. *J. Phys. Oceanogr.* **24**, 700–706.

Danabasoglu, G. & McWilliams, J. C. 1995 Sensitivity of the global ocean circulation to parameterizations of mesoscale tracer transports. *J. Phys. Oceanogr.* **25**, 2967–2987.

Eby, M. & Holloway, G. 1994 Sensitivity of a large-scale ocean model to a parameterization of topographic stress. *J. Phys. Oceanogr.* **24**, 2577–2588.

Emery, W. J., Lee, W. G. & Magaard, L. 1984 Geographic and seasonal distributions of Brunt-Väisälä frequency and Rossby radii in the North Pacific and North Atlantic. *J. Phys. Oceanogr.* **14**, 294–317.

Fyfe, J. & Marinone, G. 1995 On the role of unresolved eddies in a model of the residual currents in the central Strait of Georgia, B.C. *Atmos. Ocean* **33**, 613–619.

Gent, P. R. & McWilliams, J. C. 1990 Isopycnal mixing in ocean circulation models. *J. Phys. Oceanogr.* **20**, 150–155.

Gent, P. R., Willebrand, J., McDougall, T. J. & McWilliams, J. C. 1995 Parameterizing eddy-induced tracer transports in ocean circulation models. *J. Phys. Oceanogr.* **25**, 463–474.

Gill, A. E. 1982 *Atmosphere–Ocean Dynamics* Academic Press.

Greatbach, R. G. & Lamb, K. G. 1990 On parameterizing vertical mixing of momentum in non-eddy resolving ocean models. *J. Phys. Oceanogr.* **20**, 1634–1637.

Haidvogel, D. B., Beckmann, A., Chapman, D. C. & Lin, R.-Q. 1993 Numerical simulation of flow around a tall isolated seamount. Part II: resonant generation of trapped waves. *J. Phys. Oceanogr.* **23**, 2373–2391.

Haidvogel, D. B. & Brink, K. H. 1986 Mean currents driven by topographic drag over the continental shelf and slope. *J. Phys. Oceanogr.* **16**, 2159–2171.

Holland, W. R. 1978 The role of mesoscale eddies in the general circulation of the ocean – numerical experiments using a wind-driven quasi-geostrophic model. *J. Phys. Oceanogr.* **8**, 363–392.

Holloway, G. 1987 Systematic forcing of large-scale geophysical flows by eddy-topography interaction. *J. Fluid Mech.* **184**, 463–476.

Holloway, G. 1992 Representing topographic stress for large-scale ocean models. *J. Phys. Oceanogr.* **22**, 1033–1046.

Holloway, G. 1997 Eddy transport of thickness and momentum in layer and level models. *J. Phys. Oceanogr.* **27**, 1153–1157.

Holloway, G. & Sou, T. 1996 Measuring the skill of a topographic stress parameterization in a large-scale ocean model. *J. Phys. Oceanogr.* **26**, 1088–1092.

Kazantsev, E., Sommeria, J. & Verron, J. 1998 Subgridscale parameterization by statistical mechanics in a barotropic ocean model. *J. Phys. Oceanogr.* **28**, 1017–1042.

Marshall, J. C. 1981 On the parameterization of eddies in the ocean *J. Phys. Oceanogr.* **11**, 257–271.

McCreary, J. P. & Kundu, P. K. 1988 A numerical investigation of the Somali Current during the Southwest Monsoon. *J. Mar. Res.* **46**, 25–58.

Merryfield, W. J. 1998 Effects of stratification on quasi-geostrophic inviscid equilibria. *J. Fluid Mech.* **354**, 345–356.

Merryfield, W. J. & Holloway, G. 1997 Topographic stress parameterization in a quasi-geostrophic model. *J. Fluid Mech.* **341**, 1–18.

Nazarenko, L., Sou, T., Eby, M. & Holloway, G. 1997 The Arctic ocean/ice system, studied by contaminant modelling. *Ann. Glaciology* **25**, 17–21.

Pal, B. K. & Holloway, G. 1996 Dynamics of circulation off the westcoast of Vancouver Island. *Cont. Shelf Res.* **16**, 1591–1607.

Rhines, P. B. & Young, W. R. 1982 A theory of wind-driven circulation. I. Mid-ocean gyres. *J. Mar. Res.* **40**, 559–596.

Robert, R. & Sommeria, J. 1991 Statistical equilibrium states for two-dimensional flows. *J. Fluid Mech.* **229**, 291–310.

Robert, R. & Sommeria, J. 1992 Relaxation towards a statistical equilibrium state in two-dimensional perfect fluid dynamics. *Phys. Rev. Lett.* **69**, 2776–2779.

Salmon, R., Holloway, G. & Hendershott, M. C. 1976 The equilibrium statistical mechanics of simple quasi-geostrophic models. *J. Fluid Mech.* **75**, 691–703.

Schär, C. & Smith, R. B. 1993 Shallow-water flow past isolated topography. Part II: transition to vortex shedding. *J. Atmos. Sci.* **50**, 1401–1412.

Smith, L. T. 1992 Numerical simulations of stratified rotating flow over finite amplitude topography. *J. Phys. Oceanogr.* **22**, 686–696.

Sou, T., Holloway, G. & Eby, M. 1995 Effects of topographic stress on Caribbean Sea circulation. *J. Geophys. Res.* **101**, 16449–16453.

Thompson, L. 1995 The effect of continental rises on the wind-driven ocean circulation. *J. Phys. Oceanogr.* **25**, 1296–1316.

Treguier, A. M. 1989 Topographically generated steady currents in barotropic turbulence. *Geophys. Astrophys. Fluid Dyn.* **47**, 43–68.

Treguier, A. M., Held, I. M. & Larichev, V. D. 1997 On the parameterization of quasi-geostrophic eddies in primitive equation ocean models. *J. Phys. Oceanogr.* **27**, 567–580.

Visbeck, M, Marshall, J., Haine, T. & Spall, M. 1997 On the specification of eddy transfer coefficients in coarse resolution ocean models. *J. Phys. Oceanogr.* **27**, 381–402.

Zhang, X. & Boyer, D. L. 1993 Laboratory study of rotating, stratified, oscillatory flow over a seamount. *J. Phys. Oceanogr.* **23**, 1122–1141.

Zou, J. & Holloway, G. 1994 Entropy maximization tendency in topographic turbulence. *J. Fluid Mech.* **263**, 361–374.